



# On the morphology of elongated bubbles during their formation at submerged orifices



Kumar Gaurav<sup>a</sup>, Gaurav Mittal<sup>b</sup>, Ashish Karn<sup>b,\*</sup>

<sup>a</sup> Department of Aerospace Engineering, School of Engineering, University of Petroleum and Energy Studies, Energy Acres, Bidholi, Dehradun, Uttarakhand 248007, India

<sup>b</sup> Department of Mechanical Engineering, School of Engineering, University of Petroleum and Energy Studies, Energy Acres, Bidholi, Dehradun, Uttarakhand 248007, India

## HIGHLIGHTS

- Experiments on elongated bubbles during their formation at submerged orifices are conducted.
- Experiments are carried out on different fluids at various orifice diameters, flow rates, and orifice depth.
- Qualitative studies are done on the formation and coalescence process of bubbles.
- Quantitative analysis of the effects of various operating parameters on bubble geometry is carried out.
- Scaling laws are proposed among various governing non-dimensional parameters.
- The results may be useful for the prediction of bubble geometry based on operating parameters.

## ARTICLE INFO

### Article history:

Received 16 August 2021

Received in revised form 6 December 2021

Accepted 20 December 2021

Available online 25 December 2021

### Keywords:

Bubble formation

Scaling law

Multiphase flow

Bubble geometry prediction

Bubble morphology

Bubble coalescence

## ABSTRACT

Bubbly flow is a widely observed phenomenon in various industrial applications and has remained a topic of sustained interest over decades, owing to the complex multi-physics that govern the multiphase phenomenon. The bubble geometrical morphology and dynamics critically depend on various parameters such as flow rate, orifice diameter, working fluid properties, and height of the fluid above the orifice. Accordingly, experiments are conducted in water, acetone, and Glycerol-water solutions (10% w/w and 20% w/w) using a sub-millimeter submerged orifice of diameter 0.4 mm, 0.6 mm, and 1 mm. The volume flow rate is varied in the range of 100–300 ml per min and experiments are carried out at varying orifice depths of 4 – 12 cm. The dynamics of bubble formation is recorded by high-speed cinematography and is processed using MATLAB script. This paper presents the bubble rise and coalescence morphology and the effect of operating parameters on it. The gas injection and bubble geometrical parameters can be expressed in terms of non-dimensional numbers such as Reynolds number, Weber number, Froude number, and Eotvos number. It is found that simple scaling laws can be established among Reynolds number with Weber number, Froude number, and their ratio, which can effectively predict the bubble geometry. It is found that the relation between the ratio of Weber and Froude number to Reynolds number depends on the height of fluid above the orifice. The present work also quantifies the interconnection between Reynolds number and Eotvos number and demonstrates a relationship that is incumbent on the gas superficial velocity. In particular, it is observed that the slope of the  $Re$ - $Eo$  curve decreases with the increase in the gas superficial velocity.

© 2021 Elsevier Ltd. All rights reserved.

## 1. Introduction

The characteristic of the formation process of bubble plays a vital role in many practical applications such as boiling (Coulbaly et al. 2014; Ivey 1967), fermentation (Kheradmandnia et al. 2015), aeration (Karn et al. 2015a,b,c, 2016a), refrigeration

(Benhmidene et al. 2011), drag reduction (Karn et al. 2016b; 2017; 2018; Yoon et al. 2021), biomass energy (Rajaseenivasan and Srithar 2017) and wastewater treatment (Painmanakul et al. 2010). Indeed, a large amount of work related to bubble behavior has been done in the past (Dejonge et al., 1982; Olowson and Almstedt 1990; Fan et al. 2008; Park and Wang 2015). This extensive prior literature has mainly focused on bubble geometry (Karn et al. 2015b; Zhou et al. 2021), morphology (Calzavarini et al. 2008; Karn et al. 2015a), formation (Karn et al. 2016c), the coalescence

\* Corresponding author.

E-mail address: [akarn@ddn.upes.ac.in](mailto:akarn@ddn.upes.ac.in) (A. Karn).

process (Olmos et al. 2001; Karn et al. 2016a), mass transfer (Karn et al. 2015c) and regime classifications (Karn et al. 2016b), all of which are crucially dependent on the forces acting on the bubbles. The principal forces acting on the gas bubbles while rising in liquid are the forces of surface tension, the upward buoyant force, and drag forces. The surface tension forces usually are responsible for keeping the bubbles in their most stable shape i.e. a sphere, whereas the viscous drag force tries to deform it into a flattened shape. Further, for rising bubbles, the bubble locomotion in a region of varying pressure distribution is another important factor, whether it is caused by decreasing hydrostatic pressure distribution or the low pressure wake of advancing bubbles. Particularly, for large bubbles, the resistance force dominates over the forces of surface tension, causing them to take a highly unstable oscillating flattened shape (Roig et al. 2012). Thus, the bubble morphology is crucially governed by the magnitude of these forces, which typically depends on experimental parameters such as the gas flow rate, orifice shape and size, depth, and fluid properties. For instance, at low gas flow rates, the volume of the bubble is proportional to the surface tension and orifice radius, whereas, at high mass flow rates, the bubble volume is proportional to mass flow rate (Gerlach et al. 2007). Thus, the maximum diameter of the bubble can be predicted from the balance of surface tension, buoyancy, and drag force (Al-Hayes and Winterton 1981).

The ratio of these forces also affects the formation process of the bubble. During the formation process, the bubble size is independent of injecting gas properties and the liquid viscosity. However, the formation frequency does affect the bubble size, with higher frequencies yielding a larger bubble size. (Benzing and Myers 1955). The buoyancy forces govern the bubble rising velocity and hence also influences the bubble length. The higher bubble velocity stretches the bubble and results in a larger bubble length up to a certain limit (Agostini et al. 2008). The bubble velocity is directly proportional to the mass flow rate and vapor quality and inversely proportional to the saturation temperature. It can be expressed as a linear function of the two-phase superficial velocity (Arcanjo et al. 2010). A study by Livinus and Verdin (2021) on the inclined pipes reported that the bubble drift velocity is directly proportional to the pipe inclination and diameter, and inversely proportional to the fluid viscosity.

Apart from the bubble formation, the bubbling process can be broadly classified into other regimes as well, for instance based on the gas injection Reynolds number: single bubbling, pairing and single coalescence, double coalescence, triple bubble formation, quadruple bubble formation, coalescence at the nozzle and triple or quadruple formation, chaining, and jetting (Kyriakides et al. 1997). Similarly, Muller and Prince (1972) have conducted experiments on a single submerged orifice and divided the formation of the bubbles into six different regimes according to liquid depth and gas velocity. These six regimes are meniscus, steady jet, pulsating jet, imperfect bubble, perfect bubble, and deformed bubble.

After their formation, the bubbles rise and might merge into another bubbles forming a newer bubble of larger size. This process of bubble coalescence and has been widely studied by researchers for past several decades. The coalescence process is characterized by the formation of a neck connecting two bubbles, followed by a liquid drainage phenomenon. When the bubble coalescence is occurring away from solid walls, the neck radius is proportional to the square root of time elapsed since the moment of contact of the bubble interfaces. On the other hand, for the coalescence near the walls, the neck radius has been reported to be proportional to the 0.1 power of time since the bubble's interface contacted (Khadiya et al. 2021). The coalescence process can ordinarily occur only when the maximum liquid film length during collision is below a certain threshold limit, else the bubble collides

and bounces off without merging (Yang et al. 2019). The coalescence of two bubbles also releases the surface energy, which generates interface velocity followed by damped prolate oscillations of large amplitude (Stover et al. 1997). The coalescence process accelerates while the coalescence region shrinks with the increase in bubble approach velocity (Orvalho et al. 2021). Some studies investigating the coalescence process have also explored the effect of electrolytes on bubble coalescence and it has been observed that the rate of bubble coalescence either decreases or remains constant on the addition of electrolytes to the working liquids (Craig et al. 1993a; 1993b).

In the recent past, bubbling experiments have been very extensively researched upon, particularly under some novel scenarios. For instance, the bubbling process was experimented under high pressure and temperature, and it is noted that the pressure and temperature have a significant impact on the behavior of bubble and bubble size distribution. (Leonard et al. 2021). During the bubble experiments from the micro orifice, it is observed that the bubble formation mechanism is greatly affected by the gas kinetic energy and the capillary waves. As the bubble interface crosses its threshold value, the apex of the bubble accelerates upward and the bubble forms a prolate configuration (Mohseni et al. 2020). In experimentation with periodic bubbling- bursting, it is observed that a continuous stream of gas penetrates through a thin liquid layer and is highly associated with orifice diameter. On increasing the thickness of the liquid layer, the jet first becomes thick and small and then gradually changes to a thin and long structure (Li et al. 2019). The effect of turbulence on the bubble size and population is also studied and found to have a prominent role. In the case of larger and fewer bubbles, the vertical fluctuating velocity component plays a vital role in the turbulent stresses (Wu et al. 2021).

Clearly, a vast amount of work has been done on the topic of bubble coalescence, yet the bubble morphology during its formation at the sub-millimeter orifice is not explored deeply. Previous works were also constrained with a limited range of operating conditions and generally focused on the effect of one or two parameters rather than a comprehensive effect. Moreover, due to limitations of resources in a few of the previously reported work such as the use of syringe pump in place of the orifice cannot reflect exact industrial applications. The bubble geometry reported by previous researchers did not consider a sufficient range of data sampling, which inherits some error in the results claimed. Therefore in the present study, we have focused on the morphology of bubble rising and coalescence and the effect of various operating conditions on it. The influence of various operating parameters such as orifice size, flow rate, fluid properties, and fluid height is evaluated. Compared to previous similar work in this area, we have tried to quantify the cumulative effects of all operating parameters on bubble geometry during the formation process in terms of governing non-dimensional parameters such as Reynolds number, Weber number, Froude number, and Eotvos number. Simple scaling laws are also derived between Reynolds number and other non-dimensional parameters to predict the bubble geometry based on the operating conditions.

The current paper is structured as follows: Section 2 describes the experimental setup employed in the present study and the methodology of data collection during the experiments and its post-processing. Section 3 presents results observed in the present study and a discussion on the findings. Section 3.1 represents the qualitative results that consist of geometrical features and morphology of bubbles during the rise and coalescence process. Section 3.2 represents quantitative results that consist of the effect of individual parameters such as gas flow rate, fluid properties, and height of liquid over orifice explicitly and then the estimation of comprehensive effect in form of scaling laws of non-dimensional

number. The major conclusions of the present study are finally presented in Section 4.

## 2. Experimental setup and methodology

The experimental setup for the present study consists of a transparent rectangular tank filled with quiescent liquid and fitted with a nozzle at the bottom of the tank for injecting compressed air as shown in Fig. 1. The tank is made up of plexiglass, with a cross-sectional area of 25 cm × 25 cm, and a depth of 40 cm. In our experiments, a maximum bubble diameter of 1 cm ensures that the wide cross-section area is large enough to cause a minimal 4% confinement effect of the wall. Fig. 2 shows the schematic diagram of the experimental setup.

The geometrical morphology of the bubble depends on the viscous force, surface tension force and pressure distribution inside the bubble. Therefore, to estimate the effect of all the forces, the experiments have been done on various fluids at different mass flow rates, orifice diameters, and depths. The experiments are conducted on four different liquids i.e. water, acetone, 10% w/w glycerine water solution (Gly 10), and 20% w/w glycerine water solution (Gly 20). The properties of all the liquids are shown in Table 1:

The bubbles are generated by inserting compressed air into nozzles made up of brass with a circular orifice at the center of the top surface. Experiments are conducted using nozzles with an orifice diameter ( $d_o$ ) of 0.4, 0.6, and 1 mm. To account for the effect of depth, the study is carried out at the fluid height ( $h$ ) of 4, 8, and 12 cm above the nozzle orifice. The volume flow rate ( $\dot{Q}$ ) of the compressed air is monitored and controlled using a flow meter, and the present experiments are conducted at 100, 200, and 300 ml per min.

The images are captured at a frame rate of 5200 fps with a resolution of 1 megapixel using high-speed camera Phantom VEO 410. The camera is equipped with a telescopic lens of variable focal

length in the range of 18–36 cm to capture the zoomed-in view of the bubble. To enhance the image quality, the light is intensified using two halogen lamps placed on the other side of the camera. A diffuser sheet is used to distribute the light uniformly inside the tank. The video stream data from the camera is collected on a computer using Phantom software. The images are processed to extract the bubble dimensions using the Digital Image Processing Toolbox in MATLAB using a script that has been described by previous authors (e.g. Karn et al. 2015d). The script converts the raw image captured from high speed cinematography into binary image to detect the bubble shape (Fig. 3). Bounding box algorithm is applied on the detected bubble shape to calculate bubbles length ( $L$ ), width ( $W$ ) and aspect ratio ( $AR$ ) as shown in Fig. 4. This method of detection of bubble parameters has been extensively used by researchers in the past (Aoyama et al. 2016; Legendre et al. 2012). The dimension is averaged over at least five to ten consecutive bubbles for each case.

The physical parameters in the present study are density ( $\rho$ ) and viscosity ( $\mu$ ) of working liquid, the diameter of the orifice ( $d_o$ ), gas flow rate ( $\dot{Q}$ ), the height of liquid above orifice ( $h$ ). The superficial gas velocity at the orifice ( $U_{gs}$ ) can be calculated as  $U_{gs} = 4\dot{Q}/\pi d_o^2$ . The effective diameter ( $d_b$ ) and aspect ratio ( $AR$ ) of the bubble can be estimated as  $d_b = \sqrt{LW}$  and  $AR = L/W$  respectively, where  $L$  and  $W$  are the length and width of the bubble. These physical parameters can be represented in terms of non-dimensional parameters such as Reynolds number,  $Re = \rho U_{gs} d_b / \mu$ ; Weber number,  $We = \rho U_{gs}^2 d_b / \sigma$ ; Froude number,  $Fr = U_{gs} / \sqrt{gh}$  and Eotvos number,  $Eo = \Delta\rho g d_b^2 / \sigma$ , where  $\sigma$  is the surface tension between gas and liquid interface,  $g$  is the acceleration due to gravity and  $\Delta\rho$  is the difference between gas and liquid densities.

The flow meter was calibrated before the conduction of experiments and the uncertainty in the measurement of superficial gas velocity,  $U_{gs}$  is approximately 5.6%. The nozzle orifice diameter has a maximum uncertainty less than 0.3%. The fluid properties like density and viscosity was calculated based on the temperature

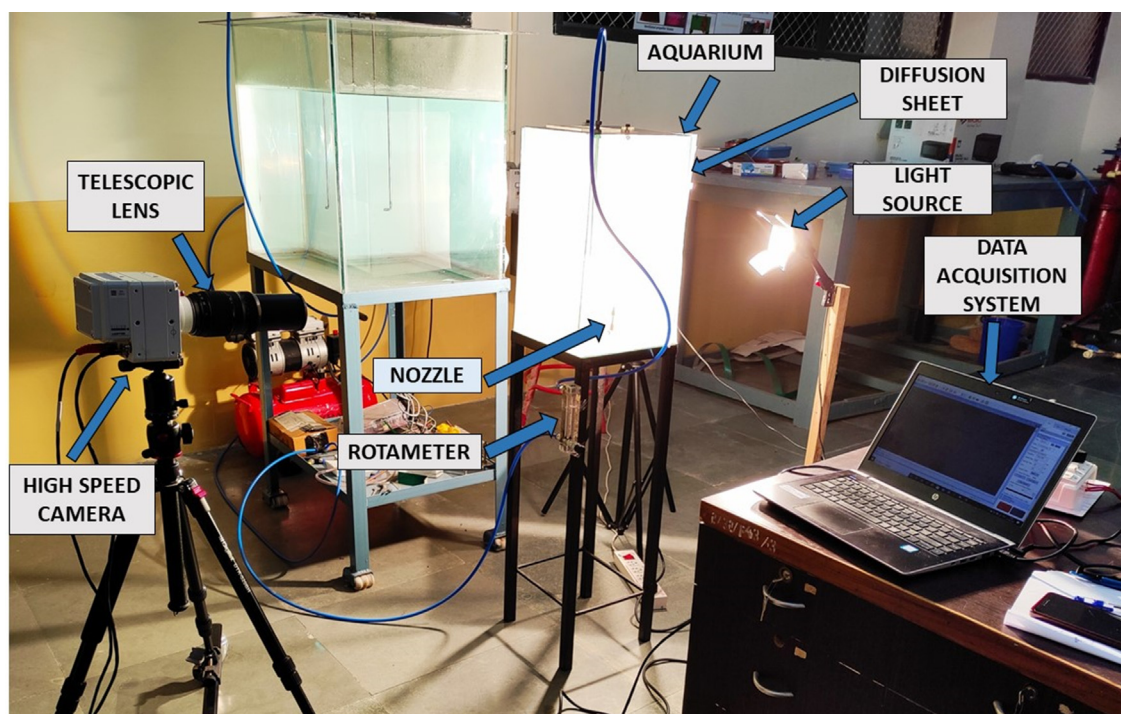


Fig. 1. The experimental setup used in the current study.

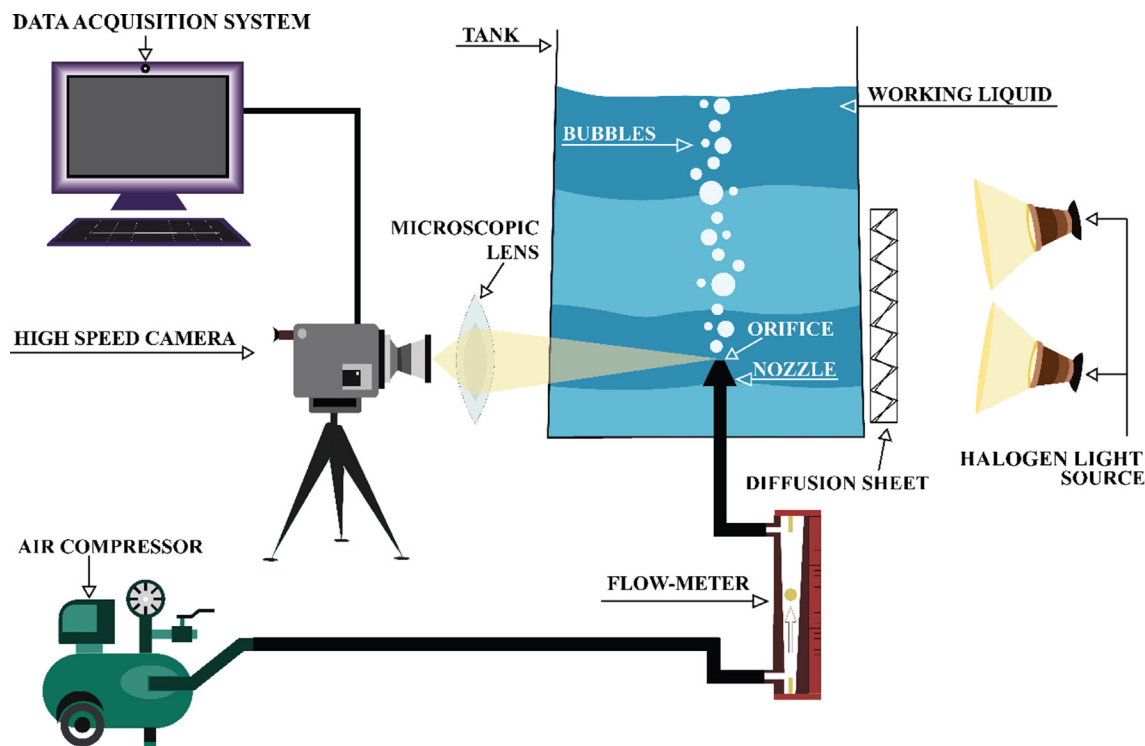


Fig. 2. Schematic diagram of the experimental setup used in the present study.

**Table 1**  
Properties of various liquids used in the present study.

| Fluid                             | Density(kg/<br>m <sup>3</sup> ) | Viscosity (mN.<br>s/m <sup>2</sup> ) | Surface tension<br>(N/m) |
|-----------------------------------|---------------------------------|--------------------------------------|--------------------------|
| Acetone                           | 784.5                           | 0.295                                | 0.02308                  |
| Water                             | 997                             | 0.8891                               | 0.07197                  |
| 10% Glycerol solution<br>(Gly 10) | 1020.6                          | 1.148                                | 0.070639                 |
| 20% Glycerol solution<br>(Gly 20) | 1045.2                          | 1.5278                               | 0.070208                 |

which was measured with an accuracy of  $\pm 0.1$  °C. The depth of the orifice is measured using a metric scale with a least count of 1 mm. Finally, in the present study, the maximum uncertainty in the calculation of,  $\hat{d}$ ,  $Re$ ,  $Fr$  and  $EO$  are estimated to be 1.6%, 6.9 %, 6.2% and 2.7 % respectively.

### 3. Results and discussion

#### 3.1. Qualitative results

In such a scenario where bubbles are produced from submerged upward orifice in a quiescent fluid, both propulsive and resistive forces act on the bubbles in the upward and downward directions, respectively. The pressure force (given by Young-Laplace equation as  $F_p = \pi d_o^2 \sigma / 4 d_b - \pi d_o^2 d_b \rho g / 4$ ), buoyancy force ( $F_b = \pi d_b^3 g \Delta \rho / 6$ ) and the gas momentum force ( $F_M = 4 \rho Q^2 / \pi d_o^2$ ), whereas the resistive forces are the viscous drag force ( $F_D = -\pi d_b^2 C_D \rho / 8 (dY/dt)^2$ ), the liquid inertia force ( $F_I = d(m_v U) / dt$ ), and the surface tension force ( $F_s = \pi \sigma d_o \sin \theta$ ). In the above expressions,  $\theta$  denote the contact angle between the bubble and the nozzle,  $m_v$  represents the added mass which is typically given as 11/16 times the product of bubble volume and the liquid density,  $U$  is the bubble rise veloc-

ity,  $Y$  is the vertical location of center of mass of the bubble and  $C_D$  is the drag coefficient of the bubble (Mohseni et al. 2020).

#### 3.1.1. Morphology during bubble rise

Fig. 5 shows the morphology of bubbles at the onset of its rise before it pinches off the nozzle. Initially, at a time duration of 6.15 ms, the shape of the bubbles are governed by a quasi-static balance between the surface tension and upward buoyant forces. The bubbles forming in the liquid initially take a conical shape as shown in Fig. 5a. This is due to the high centerline gas momentum that causes axial elongation of the bubble. The propulsive forces are greater than the resisting forces, and the bubble undergoes an unstable condition in which both the growth of the bubble and its upward motion can be seen. The stretching in the central portion continues with time, leading to a flame-like shape, while the bubble is attached to the nozzle tip via a capillary neck (Fig. 5b). Further stretching causes the bubble to pinch off from the nozzle tip and the bubble starts to rise (Fig. 5c). This motion is caused by a rapid upward movement of the capillary neck due to the surface tension force after the bubble detachment. The bubble volume is controlled by the pressure level inside the bubble and the one inside the gas reservoir. Just after the pinch-off, a series of waves is observed on the surface of the bubble. These waves travel from the bottom toward the top of the bubble and flatten the bottom surface. As the bubble ascends, the tip of the bubble blunts due to the viscous effects at the air-water interface, hence lending a bullet-like shape to the bubble (Fig. 5d). This continued frictional effect further blunts the bubble tip and hence morphs it into a wavy hemispherical shape like a spherical cap bubble (Fig. 5e). On further rising, the formation of a concave dimple on the bottom surface is observed (Fig. 5f). As the bubble rises further, another series of Kelvin-Helmholtz waves are observed on the bubble surface, but traveling from the top to the bottom surface, making a broad cross-section at the top, this provides the bubble shape of an inverted cone (Fig. 5g). The bubble oscillations continue, and the resulting viscous dissipation further flatten the bubble giving

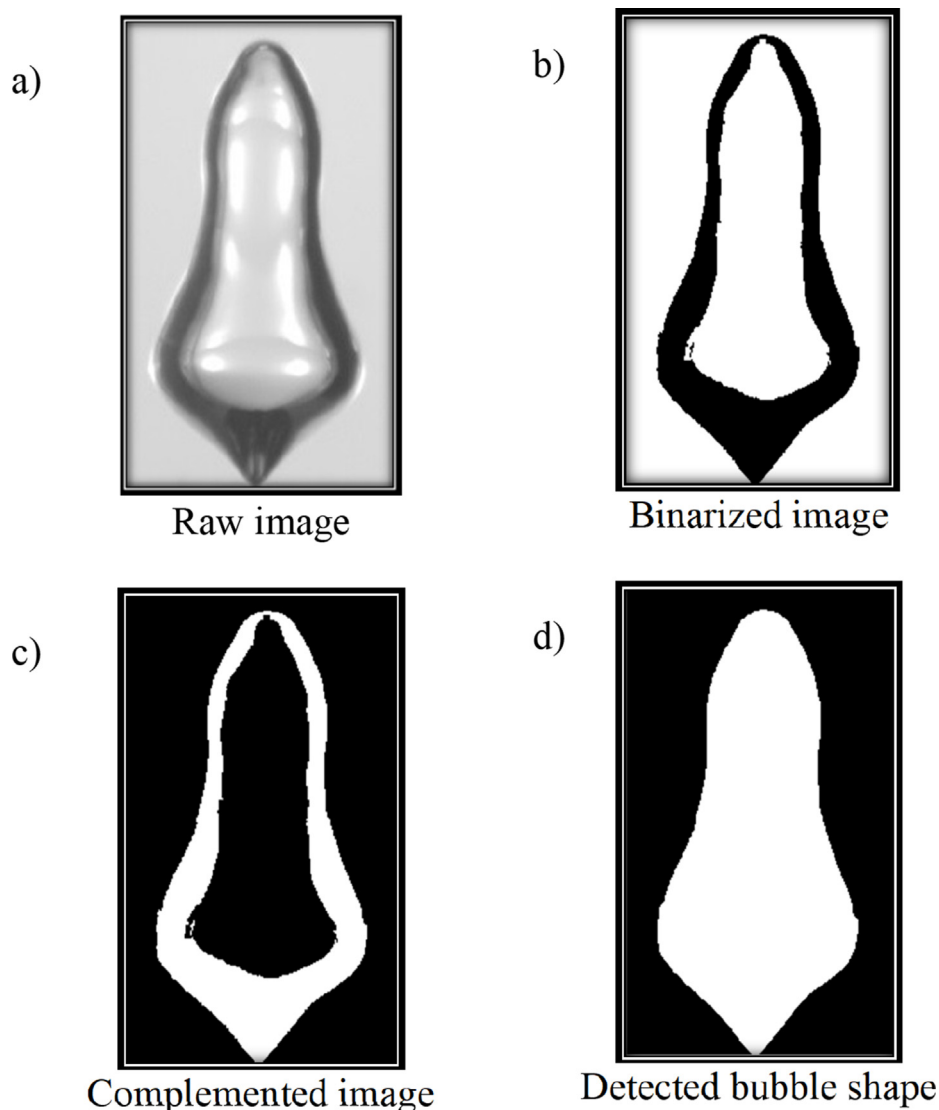


Fig. 3. Detection of bubble geometry from raw high speed images.

it a disk-like shape. (Fig. 5h), which continues to be dominated by the process of wave formation (Fig. 5i).

For small bubbles, surface tension forces are quite predominant and the pressure difference is inversely proportional to the bubble radius. Since the pressure gradients travel at the speed of sound in the gas phase, the pressure inside a small bubble is expected to be almost uniform. Because of the large pressure difference, the small bubbles possess perfect spherical symmetry and are not influenced by external disturbances. This is not the case with the large bubbles, where surface tension forces are no longer dominant (Mohseni et al. 2020). Consequently, the large bubbles are more susceptible to external fluctuations in the flow and are governed by buoyancy and inertia forces.

### 3.1.2. Bubble coalescence morphology

The morphology of ejection of the leading bubble is similar to in the case of a single bubble where it took a conical shape initially followed by a centrally elongated shape. As soon as the leading bubble pinches off, a trailing bubble interface starts to form, which influences the shape of the leading bubble. The initial shape of the trailing bubble is oval and it interacts and flattens with the lower

part of the leading bubble (Fig. 6a). Due to the low-pressure wake formed behind the leading bubble, the trailing bubble encounters lower drag forces and hence attains a higher velocity and is more elongated than the leading bubble (Fig. 6b). The trailing bubble strikes the flattened lower surface of the leading bubble and creates a concave dimple on it (Fig. 6c). With the passage of time, the leading bubble morphs into a disk shape whereas the trailing bubble turns to an almost spherical shape due to the action of viscous forces (Fig. 6d). The trailing bubble starts coalescing into the leading bubble, forming a neck connecting both the bubbles. The neck formation is associated with the formation of two sets of waves, one moves upward into the leading bubble while the other travels downwards into the trailing bubble (Fig. 6e). The air from the trailing bubble then passes to the leading bubble through the connecting neck due to the buoyancy effect, creating a reverse truncated shape of the coalesced bubble (Fig. 6f). A couple of jets are formed from the upper and lower surface, the jet from the bottom surface is thinner and longer than that of the upper surface (Fig. 6g). The collision of the jet emerges from the bottom surface, into the upper surface, creating multiple strong surface waves. This water jet forces the upper surface to move faster than the bubble

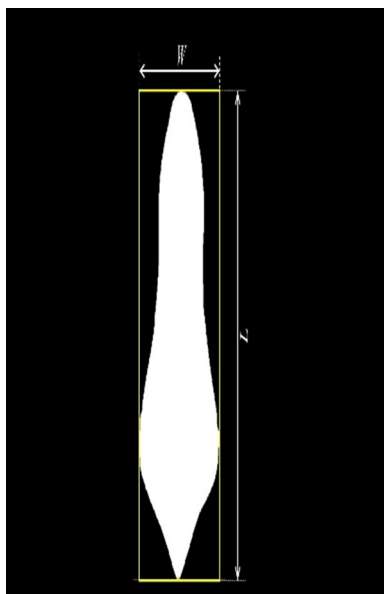


Fig. 4. Evaluation of bubble length ( $L$ ) and width ( $W$ ) using the bounding box algorithm.

velocity, thus creating a sharp leading edge and morphs the coalesced bubble into a wavy conical shape (Fig. 6h). Further action of friction forces increases the bluntness of the bubble, providing it the shape of a wavy disk (Fig. 6i).

### 3.2. Quantitative results

For quantitative analysis of the bubble formation, the experimental images at various time intervals are extracted from high-speed cinematography. The images are processed using an in-house developed MATLAB algorithm to extract bubbles' geometrical parameters. Assuming the bubble to be an ellipse, the minor and major axis diameter of the bubble are estimated using a bounding box algorithm. The diameter of the bubble is then computed by taking the geometric mean of the minor and major diameters. This methodology is applied to estimate the diameter of at least five to ten consecutive bubbles for each case. The average of these diameters is considered as the final diameter of the bubble for that case. This diameter is used to calculate forces on the bubble in terms of non-dimensional numbers.

The dynamics of elongated bubble formation are driven primarily by viscous force, buoyancy, surface tension, inertial force and thus can be recast in terms of non-dimensional parameters. Reynolds number plays an important role in the bubble shape during formation by accounting for the ratio of inertial and viscous forces. Since the surface tension plays a crucial role in the bubble formation process, the Weber number is also taken into account. The gravitational and buoyancy force stretches the bubble and alters its aspect ratio. These effects are taken into account by monitoring the Froude number and Eotvos number. The non-dimensional numbers are determined for each case and are plotted against each other to find out a scaling relation between them. These relations can be helpful in the prediction of bubble geometry during formation.

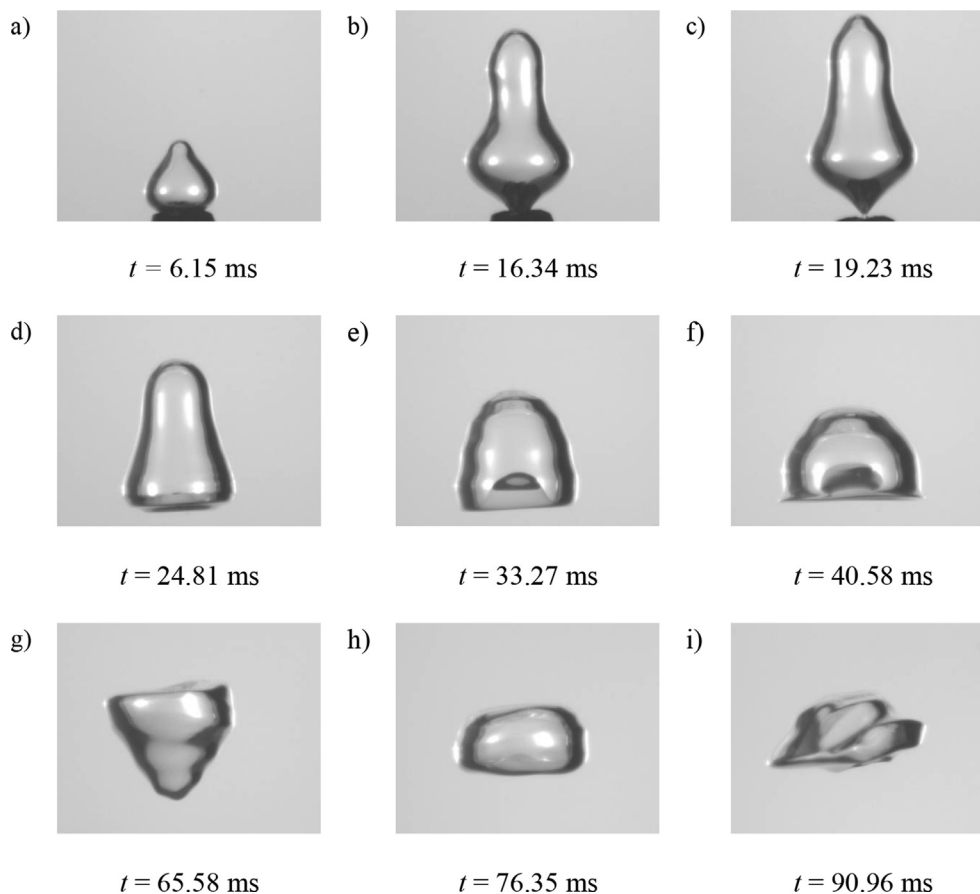
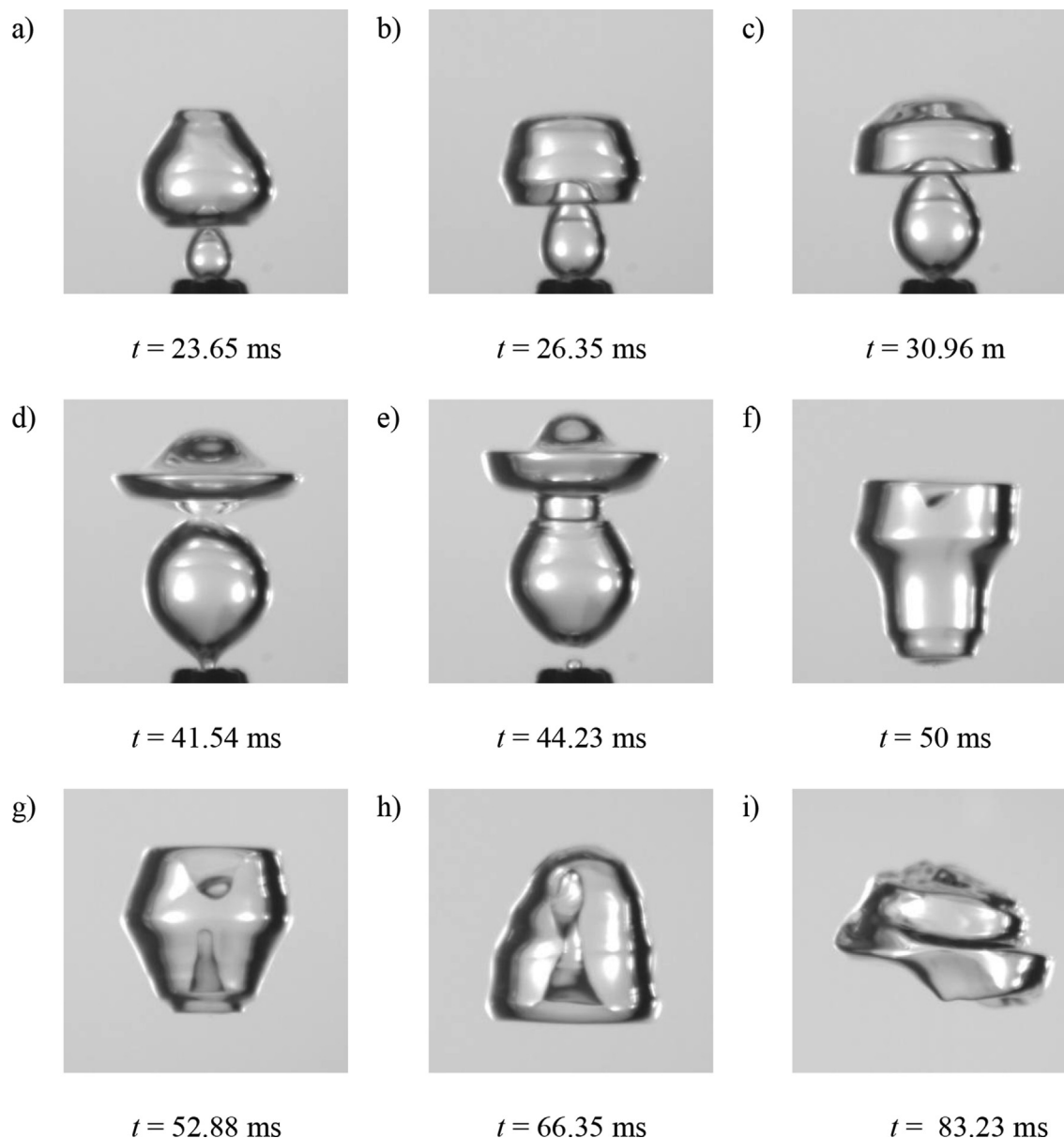


Fig. 5. Bubble geometry and morphology during rising at different time intervals ( $t$ ). Similar morphology of bubble was observed for all the cases.



**Fig. 6.** Bubble coalescence morphology at different time instances. Similar pattern of coalescence was observed for all the cases.

### 3.2.1. Effect of gas superficial velocity on bubble geometry

The gas superficial velocity has a significant impact on the bubble length. The gas superficial velocity can be increased either by increasing the volume flow rate of the gas or by decreasing the orifice diameter. At a constant orifice diameter, any rise in volume flow rate results in a proportional rise in the gas superficial velocity which further cause an elongation of the bubble as shown in Fig. 7a. However, the variation in width is relatively negligible and thus an augmentation in the bubble aspect ratio is observed. However, at a fixed volume flow rate, the gas superficial velocity shows an increment upon a reduction in the orifice diameter. In such cases, the bubble length reduces with an enhancement in the gas superficial velocity. Fig. 7b shows the increase in bubble diameter with decrease in gas superficial velocity, which in turn can be attributed to the increase in orifice diameter. However the width almost remains constant, consequently, a decrease in aspect ratio is also observed as shown in Fig. 8.

Fig. 8 illustrates the dependence of bubble height as well as the bubble aspect ratio on the orifice diameter, or alternatively, the gas

superficial velocity. For all the liquids used in our experiments, the bubble size is noted to increase as the orifice diameter is increased. In accordance with the continuity principle, this can alternatively be stated as the inverse dependence of the bubble size upon the gas superficial velocity. At an orifice diameter of  $0.4 \mu\text{m}$ , the bubble sizes lie in the range of 5–6 mm, at an orifice diameter of  $0.6 \mu\text{m}$ , in the range of 8–9 mm, and finally bubble sizes of approximately 12 mm are obtained for an orifice diameter of  $1 \mu\text{m}$ . Conversely, a decreasing trend is observed with respect to aspect ratio: at a smaller orifice size of  $0.4 \mu\text{m}$ , a near spherical bubble with a mean aspect ratio around 1.25 is obtained. This mean aspect ratio increases to 1.55 and 1.8, for orifice sizes of  $0.6 \mu\text{m}$  and  $1 \mu\text{m}$ , respectively.

### 3.2.2. Effect of fluid depth on bubble geometry

The effect of fluid depth on bubble geometry varies with respect to experimental conditions, most noticeably on the orifice diameter. For the larger orifice diameter, the bubble size decreases with an increase in orifice depth as shown in Fig. 9b. However, for lower

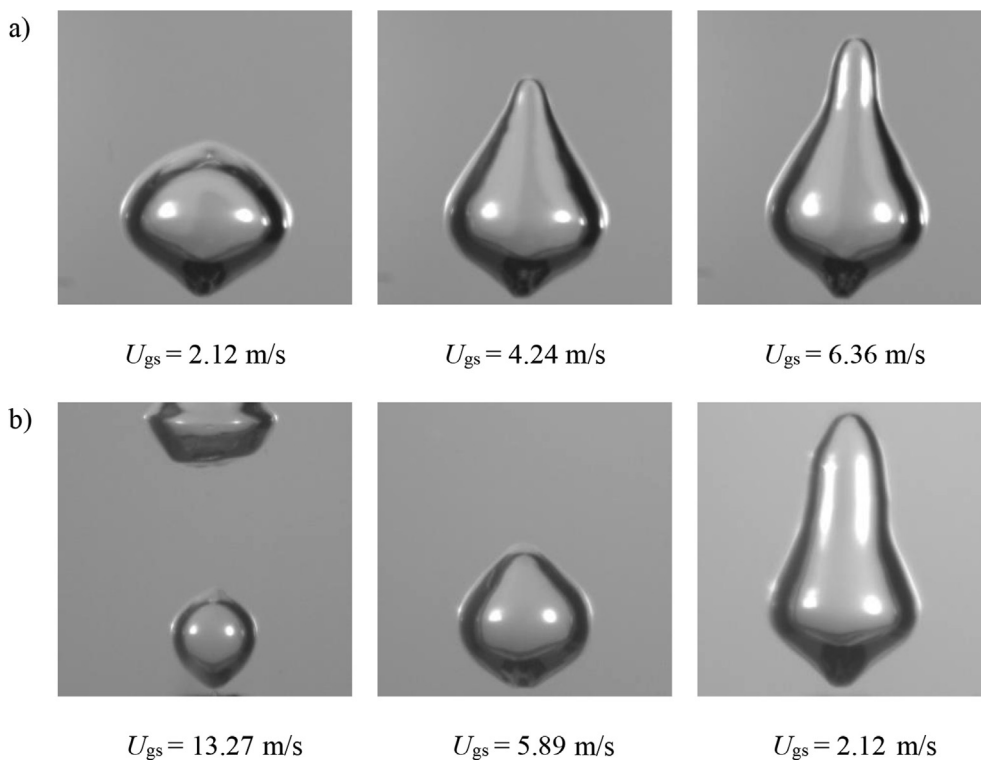


Fig. 7. Bubble geometrical changes due to change in gas superficial velocity through (a) increasing flow rate, (b) increasing orifice diameter. Note that the velocity changes in part (b) simply correspond to the increasing orifice area of the nozzle.

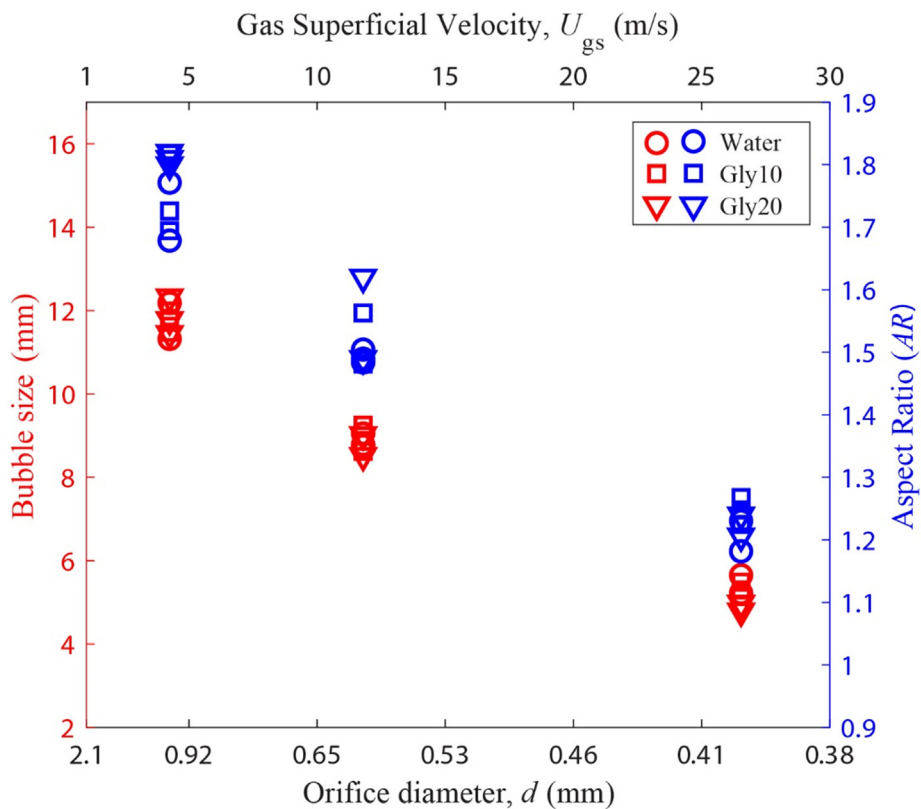


Fig. 8. Effect of variation in the bubble height (in red), and bubble aspect ratio (in blue) with the orifice diameter or its corresponding superficial gas velocity (shown on the top horizontal axis). (For interpretation of the references to colour in this figure legend, the reader is referred to the web version of this article.)

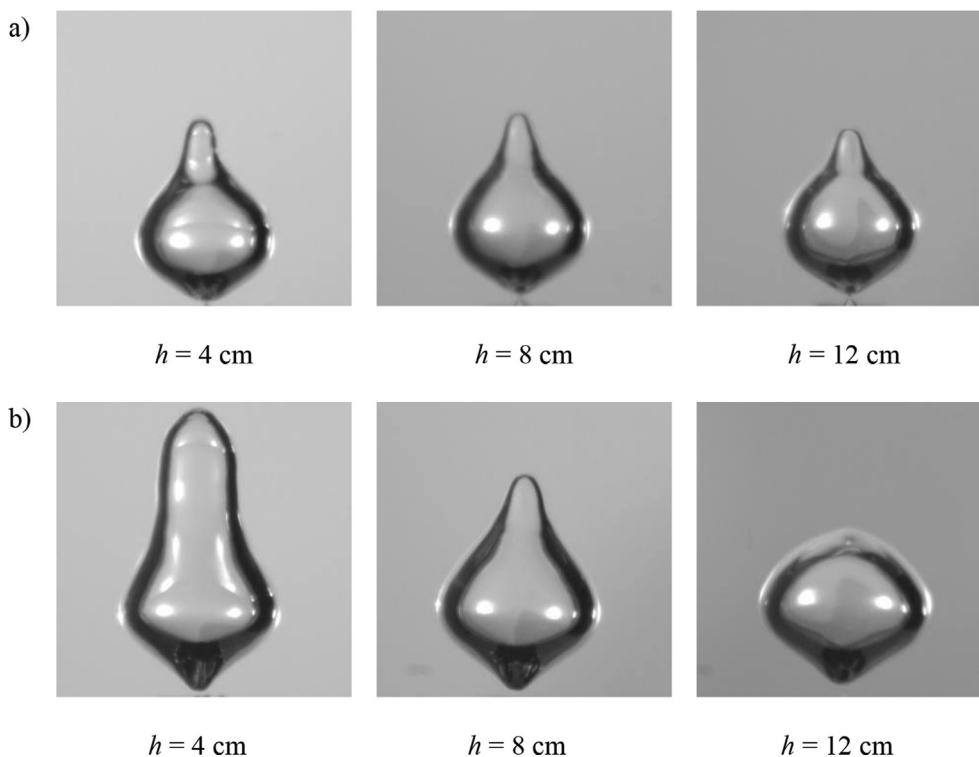


Fig. 9. Effect of depth on bubble geometry at orifice diameter of (a) 0.6 mm and (b) 1 mm.

orifice diameter, the effect diminishes and almost equal size bubbles are formed at all fluid depths as shown in Fig. 9a. However, the bubble width is almost unaffected by the liquid depth. Consequently, the aspect ratio also follows the same trend as the length of the bubble. Fig. 9 also shows that for constant volume flow rate at a specific depth, the length and hence volume of the bubble is greater for larger orifice diameter. Therefore, the frequency of bubble formation is lower in the case of higher orifice diameter.

As seen above, the aspect ratio of the bubble depends on the orifice diameter and the depth of the orifice. To further explore this variation, a non-dimensional number  $\hat{d}$  is defined as  $\hat{d} = \frac{d_o}{h} * 10^3$ .

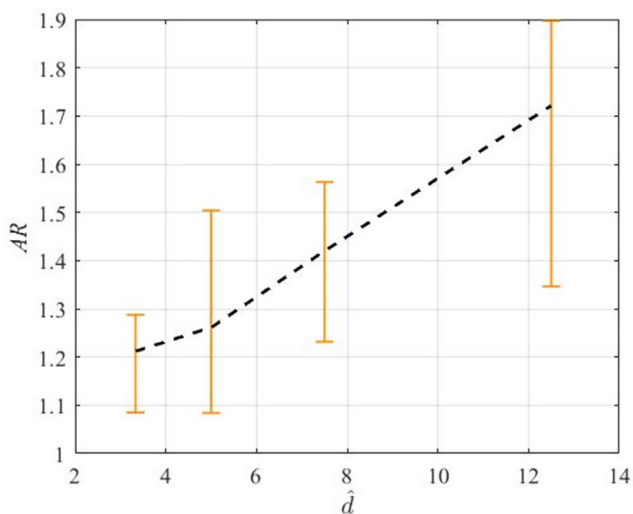


Fig. 10. Variation of mean bubble aspect ratio with non-dimensional parameter  $\hat{d}$ . The vertical bars don't represent the standard deviation in the measurement of AR. Rather, it denotes the range of variation of AR that is observed across all recorded cases at a particular value of  $\hat{d}$ .

The aspect ratio of the bubble is plotted against  $\hat{d}$  and is shown in Fig. 10. At a particular  $\hat{d}$ , the data collected for all the cases are denoted by employing the vertical error bars, and later the mean value at each  $\hat{d}$  is joined using a dashed line, suggesting a preliminary trend in the variation of AR. It can be clearly inferred that the mean value of aspect ratio increases almost linearly with increase in  $\hat{d}$ . Put simply, large aspect-ratio bubbles are generated more readily with larger orifices and this behaviour is more prominently noticeable at lower water depths.

### 3.2.3. Effect of fluid properties on bubble geometry

The bubble formed in the acetone medium is the smallest and has an oval shape with pointed ends as shown in Fig. 11a. Due to the small volume of bubbles, the frequency of bubble generation is greatest in acetone. In most of the cases of acetone, it is observed that as soon as the leading bubble detaches, multiple small trailing bubbles erupt and strike the leading bubble which then bounced back without coalescence. For a few cases, such as at an orifice diameter of 1 mm and a flow rate of 100 ml per min, single bubbling is observed. In chaotic bubbling, there is a significant difference in the geometry of bubbles, therefore these cases are omitted from the scaling law analysis. In water, a nearly spherical-shaped bubble is formed with a diameter that is approximately equal to the length of bubbles in acetone at the same experimental conditions (Fig. 11b). In both Water-Glycerine solutions, a highly elongated bubble is formed with a size quite larger than in the case of water and acetone as shown in Fig. 11c and 11d. The longest bubble is observed in Gly 10. It is also found out that the dependence of the geometry of the bubble can't be extricated with respect to the density or viscosity of the liquid, rather it depends on all the fluid properties. Therefore to suitably understand and predict the variation of bubble geometry with the fluid properties, a detailed study is presented in the following sections.

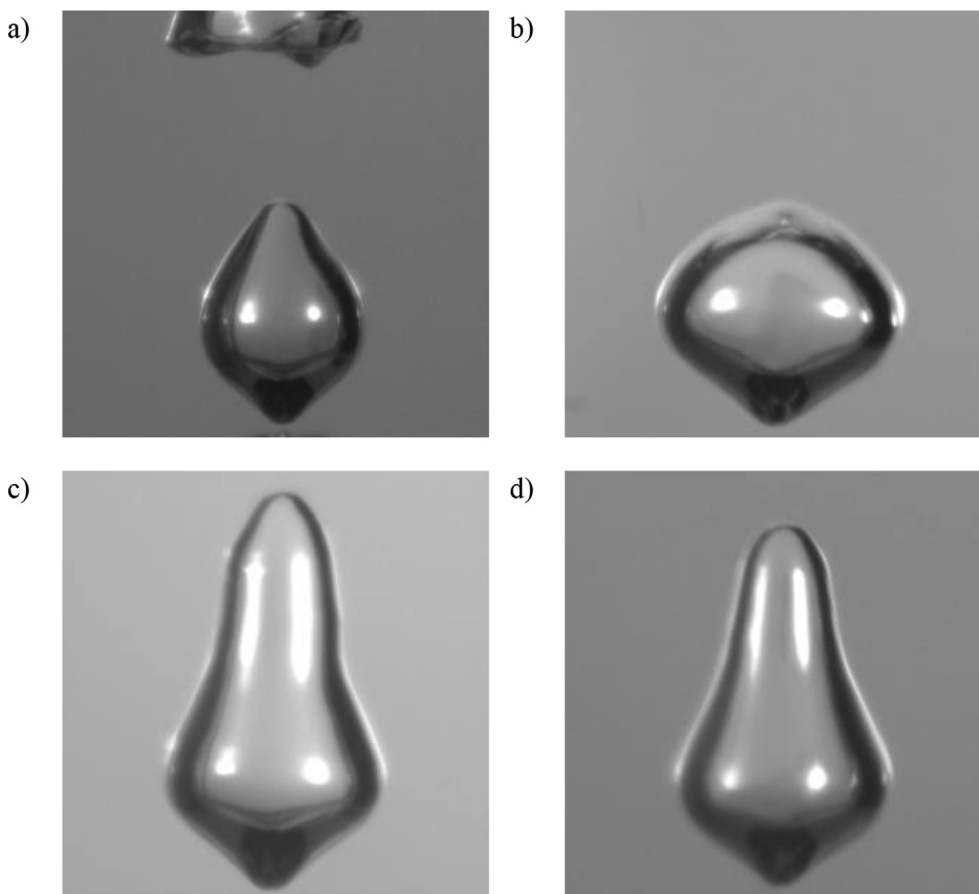


Fig. 11. Bubble geometry just after pinch-off in various liquids (a) Acetone, (b) Water, (c) Gly 10, (d) Gly 20.

3.2.4. The inter-relationships between inertia, surface tension and viscous forces: Re-We scaling

It is well understood that the liquid surface tension tries to keep the bubble in a more stable form (and thereby, closer to a spherical shape) whereas the viscous effects flatten the bubble. Therefore the

final shape of the bubble during the formation process critically depends on the balance between these two forces. To quantify this effect, Reynolds number and Weber number are estimated based on bubble geometry just after the pinch-off. The Reynolds number varied over the range of 16,000 – 155,000, whereas the Weber number varied from 430 to 51,500. The values are plotted against each other to derive a scaling law between Reynolds number and Weber number, which can predict the effect of viscous and surface tension forces on bubble formation geometry as shown in Fig. 12. The figure clearly shows that the Reynolds number and Weber number follow a parabolic law i.e. on increasing the Reynolds number, the Weber number increases slightly higher than the square of the Reynolds number. The increase in Reynolds number is associated with either an increase in inertial force or a decrease in viscous force. Weber number is also directly proportional to the inertial force, hence, it increases with an increment in Reynolds number. Put simply, when the inertial forces are predominant over the viscous forces (at high Re), in such a scenario, the weak surface tension forces are also susceptible to be overpowered by it. The exact dependence is found out by regression analysis as,

$$We = 2.98 * 10^8 * Re^{2.364} \tag{1}$$

This relation quantifies the cumulative effect of injection parameters such as orifice diameter and gas flow rate and fluid properties on the bubble size.

3.2.5. The inter-relationships between inertial, viscous, and gravitational forces: Re-Fr scaling

Gravity also plays an important role in the determination of geometrical characteristics of bubbles during their formation. The

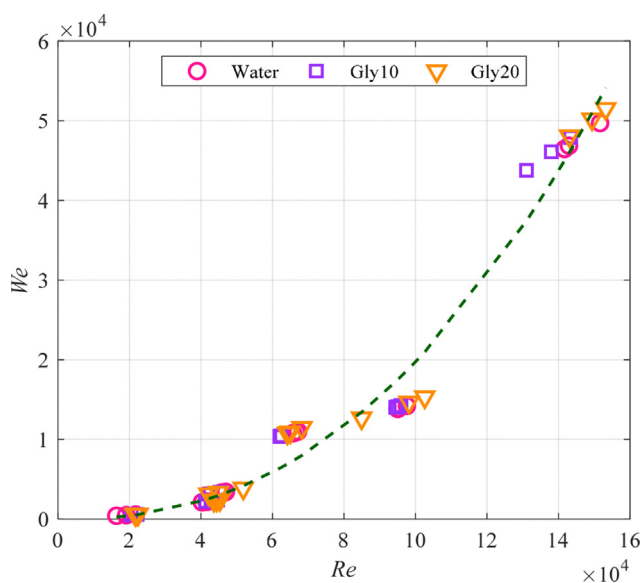
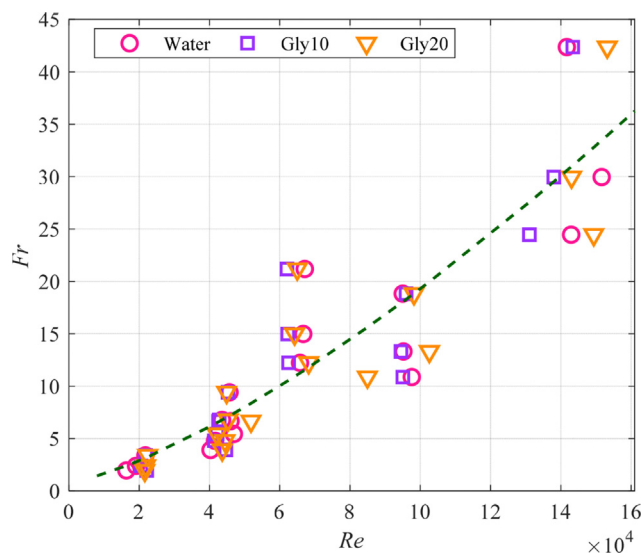


Fig. 12. Reynold number and Weber number relation for bubbles just after pinch-off. Curve fitting RMSE value = 2557, R squared value: 0.976.



**Fig. 13.** Reynold number and Froude number relation for bubble just after pinch-off. Curve fitting RMSE value = 4.69, R-squared value: 0.815.

effect of gravity can be taken into account by including the Froude number in this scaling analysis, since it is the measure of the ratio of inertial and gravitational forces. Fig. 13 shows the plot between the Froude number and the Reynolds number. The nature of this dependence may yield crucial insight into the determination of the bubble velocity and length. As per Fig. 13, there is an almost linear relation between Froude and Reynolds number.

$$Fr = 2.67 \times 10^{-6} * Re^{1.368} + 0.854 \quad (2)$$

It is evident from the relation that an increase in Reynolds number consequently also increases the Froude number. This is because an increase in the inertial forces increases the bubble size which results in a higher gravitational force on the bubble that increases both Reynolds number and Froude number. On the contrary, an increment in the viscous forces leads to greater shearing forces or smaller size bubbles which are characterized by lesser magnitude of gravitational forces and hence a smaller Froude number.

### 3.2.6. The inter-relationships between the relevant forces: A new scaling law.

It is clear from the previous graphs that the  $Re$ ,  $We$ , and  $Fr$  have a prominent effect on the bubble geometry during the formation process. However, the  $Re$ - $We$  relation underscores the effect of viscous and surface tension forces only. On the other hand,  $Re$  -  $Fr$  relationship highlights the effects of viscosity and gravity. It can also be clearly observed that the scaling law between Froude number and Reynolds number is rather discrepant with a smaller R-squared value equaling 0.815. This suggests the need for a better scaling law that can accurately capture the physics of the formation process. Such a scaling law must incorporate the aggregate effects of the inertial force, viscous force, surface tension, and gravitational force. In order to explore such a scaling law, the ratio of  $We$  to  $Fr$  is plotted against  $Re$ , and shown in Fig. 14. When the results are plotted in such a fashion, interestingly the data corresponding to all three fluids converge on one single straight line, with a very precise value of R-square greater than 0.999. It is evident from Fig. 14 that there are three different lines of varying slopes, and each line represents a particular depth of bubble formation. A scaling law shows that the  $Re$  is linearly proportional to the  $We/Fr$  and can be expressed as  $We/Fr = m * Re + c$ , and the slope of the line ( $m$ ) depends on the depth of the orifice from the surface of the water. All the regression coefficients for different

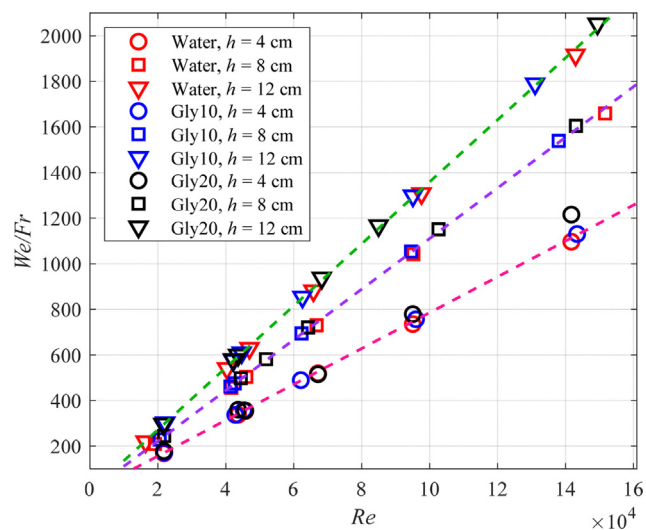


**Fig. 14.** Variation in ratio of Weber to Froude number with Reynold number. Curve fitting details: (a)  $h = 4$  cm: RMSE = 7.07, R squared = 0.999, (b)  $h = 8$  cm: RMSE = 10.14, R squared = 0.999, (c)  $h = 12$  cm: RMSE = 12.09, R squared = 0.999.

**Table 2**  
Regression coefficients for different heights.

| Depth of orifice<br>$h$ (m) | Regression coefficients |         |
|-----------------------------|-------------------------|---------|
|                             | $m$                     | $c$     |
| 0.04                        | 0.00786                 | -0.4826 |
| 0.08                        | 0.0111                  | 0.6193  |
| 0.12                        | 0.0134                  | 0.3954  |

heights are shown in Table 2 that shows the slope of the line ( $m$ ) increases as the liquid height ( $h$ ) increases. A relation has also been derived between depth of orifice ( $h$ ) and the slope of the line ( $m$ ) as shown below:

$$m = 0.06925h + 0.005247 \quad (3)$$

### 3.2.7. The inter-relationship between Reynolds number and Eotvos number

The buoyancy force is also crucial in bubble rise velocity and hence bubble length. To account for the buoyancy effect, the Eotvos number is also estimated and analyzed. The Eotvos number is plotted against Reynolds number, to quantify the combined effect of inertial, viscous, buoyancy, and surface tension force. It is found that the Eotvos number is directly proportional to the Reynolds number as shown in Fig. 15. It can be depicted that higher inertial forces resulted in the formation of larger bubbles that possess a higher force of buoyancy than the smaller bubbles. Therefore, an increase in Reynolds number also increases the value of the Eotvos number. Again, by fitting a curve to the experimental data shows that the relation can be expressed as  $Eo = m * Re + c$ . However, the value of  $m$  and  $c$  depends on the gas superficial velocity and is tabulated in Table 3. For higher gas superficial velocities, the value of  $m$  is lower i.e. increment in Reynolds number gradually increases Eotvos number, due to decrease in inertial force and vice versa. It may also be concluded that at higher gas superficial velocity, the gravitational and viscous forces are dominant, whereas at low gas superficial velocity the bubble formation phenomenon is surface tension driven. Further, another interconnecting relation between the regression coefficients and the gas superficial velocity has been derived using interpolation method as

$$m = 2.5 \times 10^{-3} * U_{gs}^{-1.25} \quad (5)$$

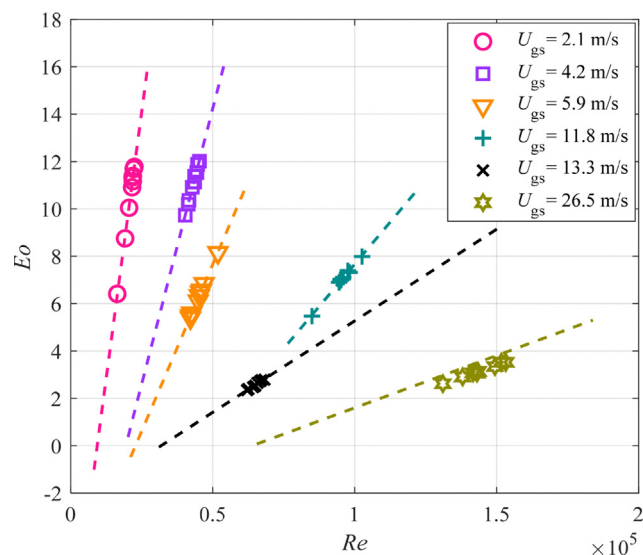


Fig. 15. Reynold number and Eotvos number relation for bubbles just after pinch-off.

Table 3  
Regression coefficients for different gas superficial velocity.

| Gas superficial velocity<br>$U_{gs}$ | Regression coefficients |        |
|--------------------------------------|-------------------------|--------|
|                                      | $m$                     | $c$    |
| 2.1 m/s                              | $9 \times 10^{-4}$      | -8.377 |
| 4.2 m/s                              | $4.65 \times 10^{-4}$   | -9     |
| 5.9 m/s                              | $2.81 \times 10^{-4}$   | -6.408 |
| 11.8 m/s                             | $1.42 \times 10^{-4}$   | -6.566 |
| 13.3 m/s                             | $7.73 \times 10^{-5}$   | -2.455 |
| 26.5 m/s                             | $4.15 \times 10^{-5}$   | -2.819 |

#### 4. Conclusions

The current paper reports the geometrical morphology of bubbles during formation, rising, and coalescence in different fluids at three different orifice sizes. Each orifice is provided with a range of mass flow rates at different heights. We have also studied the effect of these parameters explicitly on the geometry of bubbles during the formation. These parameters are then expressed in form of non-dimensional numbers such as Reynolds number, Weber number, Froude number, and Eotvos number. Simple scaling law is derived between Reynolds number and other non-dimensional parameters to quantify the influence of various forces on the bubble geometry. The scaling law can effectively predict the bubble geometry for a given set of experimental conditions. The major findings of the current manuscript can be summarized as follows:

- During the rising process, the shape of the bubble changes from an elongated cone to a bullet, to a hemisphere, and then to an inverted cone and finally a disk. A concave dimple is observed on the bottom of the bullet and hemispherical shape. A series of surface waves traveling from bottom to top is observed during pinch off which makes the surface of the bubble wavy and later causes the bubble to take an inverted cone shape.
- The leading bubble emerged similar to a single bubble initially followed by the formation of a trailing bubble. Both the bubbles interfere and thus affect each other's geometry. The trailing bubble is faster and becomes more elongated due to the wake of the leading bubble whereas a dimple is imprinted by the trailing bubble on the bottom surface of the leading bubble. A neck is formed at the contact point of the bubbles during coales-

cence. The neck formation is associated with the formation of two sets of waves, one set traveling upward into the leading bubble and the other down into the trailing bubble. Just after the coalescence, a couple of jets are also observed from the bottom and top surface of the coalesced bubble.

- The bubble length and aspect ratio during formation increases with an increase in gas flow rate, and decrease in orifice diameter. The effect of fluid height on bubble length and aspect ratio depends on the orifice size. For larger orifice size (1 mm diameter), the bubble length increases with a decrease in fluid height above orifice, for smaller orifice (0.6 and 0.4 mm diameter) the bubble length is almost constant for all fluid height.
- The shape of the bubble depends on the relative magnitudes of viscous force, surface tension force and forces due to pressure distribution, and therefore a relation between weber number and Reynolds number is established. It is found that Weber number is directly proportional to the square of Reynolds number and can be estimated as  $We = 2.98 \times 10^8 * Re^{2.364}$ .
- To account for the effect of gravity on bubble geometry, the scaling law between Froude number and Reynold number is found as  $Fr = 2.67 \times 10^{-6} * Re^{1.368} + 0.854$ . Based on the scaling law, it is concluded that for a lower value of inertial forces, the bubble geometry is dependent majorly on gravitational forces than viscous forces. As the inertial force rises, the viscous force starts to dominate the bubble geometry than gravitational forces.
- It is found that the ratio of Weber number to Froude number has a linear relation with Reynold number and can be expressed in as  $We/Fr = m * Re + c$ . However, the slope of the curve depends on the height of fluid above the orifice and can be estimated by using the relation  $m = 0.06925h + 0.005247$
- The Eotvos number depends linearly on the Reynolds number, and the slope of the  $Re-Eo$  curve is inversely proportional to the gas superficial velocity. The slope of the  $Re-Eo$  curve can be estimated as  $m = 2.5 \times 10^{-3} * U_{gs}^{-1.25}$
- The liquid temperature also affects the bubble formation morphology and therefore the effect of liquid temperature on the proposed scaling law can also be investigated in future studies.

#### CRedit authorship contribution statement

**Kumar Gaurav:** Conceptualization, Methodology, Data curation, Writing – original draft. **Gaurav Mittal:** Software. **Ashish Karn:** Conceptualization, Data Analysis, Supervision, Funding acquisition, Writing – review & editing.

#### Declaration of Competing Interest

The authors declare that they have no known competing financial interests or personal relationships that could have appeared to influence the work reported in this paper.

#### Acknowledgments

Authors acknowledge the support received from Early Career Research Award, Science and Engineering Research Board, Department of Science and Technology, India under the grant no. ECR/2017/002945, as well as the support received under UPES-SEED grant program from the University of Petroleum and Energy Studies.

#### References

- Agostini, B., Revellin, R., Thome, J.R., 2008. Elongated Bubbles in Microchannels. Part I: Experimental Study and Modeling of Elongated Bubble Velocity. International

- Journal of Multiphase Flow 34 (6), 590–601 <https://www.sciencedirect.com/science/article/pii/S030193220700198X>.
- Al-Hayes, R.A.M., Winterton, R.H.S., 1981. Bubble Diameter on Detachment in Flowing Liquids. *International Journal of Heat and Mass Transfer* 24 (2), 223–230 <https://www.sciencedirect.com/science/article/pii/0017931081900302>.
- Arcanjo, A.A., Tiberiça, C.B., Ribatski, G., 2010. Evaluation of Flow Patterns and Elongated Bubble Characteristics during the Flow Boiling of Halocarbon Refrigerants in a Micro-Scale Channel. *Experimental Thermal and Fluid Science* 34 (6), 766–775 <https://www.sciencedirect.com/science/article/pii/S0894177710000087>.
- Aoyama, S., Hayashi, K., Hosokawa, S., Tomiyama, A., 2015. Shape of ellipsoidal bubbles in infinite stagnant liquids. *International Journal of Multiphase Flow* 79. <https://doi.org/10.1016/j.ijmultiphaseflow.2015.10.003>.
- Benhmide, A., Chaouachi, B., Gabsi, S., 2011. Effect of Operating Conditions on the Performance of the Bubble Pump of Absorption-Diffusion Refrigeration Cycles. *Thermal Science* 15 (3), 793–806.
- Benzing, R.J., Myers, J.E., 1955. Low Frequency Bubble Formation at Horizontal Circular Orifices. *Industrial & Engineering Chemistry* 47 (10), 2087–2090. <https://doi.org/10.1021/ie50550a022>.
- Calzavarini, ENRICO, Kerscher, MARTIN, Lohse, DETLEF, Toschi, FEDERICO, 2008. Dimensionality and morphology of particle and bubble clusters in turbulent flow. *Journal of fluid mechanics* 607, 13–24.
- Coulibaly, A., Bi, J., Lin, X., Christopher, D.M., 2014. Effect of Bubble Coalescence on the Wall Heat Transfer during Subcooled Pool Boiling. *International Journal of Thermal Sciences* 76, 101–109 <https://www.sciencedirect.com/science/article/pii/S1290072913002159>.
- Craig, V.S.J., Ninham, B.W., Pashley, R.M., 1993a. Effect of Electrolytes on Bubble Coalescence. *Nature* 364 (6435), 317–319. <https://doi.org/10.1038/364317a0>.
- Craig, V.S.J., Ninham, B.W., Pashley, R.M., 1993b. The Effect of Electrolytes on Bubble Coalescence in Water. *The Journal of Physical Chemistry* 97 (39), 10192–10197. <https://doi.org/10.1021/j100141a047>.
- Dejonge, R., Barendrecht, E., Janssen, L., Vanstralen, S., 1982. Gas Bubble Behaviour and Electrolyte Resistance during Water Electrolysis. *International Journal of Hydrogen Energy* 7 (11), 883–894.
- Fan, X., Yang, Z., Parker, D.J., Armstrong, B., 2008. Prediction of Bubble Behaviour in Fluidised Beds Based on Solid Motion and Flow Structure. *Chemical Engineering Journal* 140 (1–3), 358–369.
- Gerlach, D., Alleborn, N., Buwa, V., Durst, F., 2007. Numerical Simulation of Periodic Bubble Formation at a Submerged Orifice with Constant Gas Flow Rate. *Chemical Engineering Science* 62 (7), 2109–2125 <https://www.sciencedirect.com/science/article/pii/S0009250907000292>.
- Ivey, H.J., 1967. Relationships between Bubble Frequency, Departure Diameter and Rise Velocity in Nucleate Boiling. *International Journal of Heat and Mass Transfer* 10 (8), 1023–1040 <https://www.sciencedirect.com/science/article/pii/0017931067901184>.
- Karn, A., Ellis, C., Hong, J., Arndt, R.E.A., 2015a. Investigations into the turbulent bubbly wake of a ventilated hydrofoil: moving toward improved turbine aeration techniques. *Experimental Thermal and Fluid Science* 64, 186–195.
- Karn, A., Ellis, C., Milliren, C., Hong, J., Scott, D., Arndt, R., Gulliver, J., 2015b. Bubble size characteristics in ventilated hydrofoils with two aeration configurations. *International Journal of Fluid Machinery and Systems* 8 (2), 73–83.
- Karn, A., Monson, G.M., Ellis, C.R., Hong, J., Arndt, R.E.A., Gulliver, J.S., 2015c. Mass transfer studies across ventilated hydrofoils: A step towards hydroturbine aeration. *International Journal of Heat and Mass Transfer* 87, 512–520.
- Karn, A., Ellis, C., Arndt, R., Hong, J., 2015d. An integrative image measurement technique for dense bubbly flows with a wide size distribution. *Chemical Engineering Science* 122, 240–249.
- Karn, A., Shao, S., Arndt, R.E.A., Hong, J., 2016a. Bubble coalescence and breakup in turbulent bubbly wake of a ventilated hydrofoil. *Experimental Thermal and Fluid Science* 70, 397–407.
- Karn, A., Arndt, R.E.A., Hong, J., 2016b. An experimental investigation into supercavity closure mechanisms. *Journal of Fluid Mechanics* 789, 259–284.
- Karn, A., Arndt, R.E.A., Hong, J., 2016c. Gas entrainment behaviors in the formation and collapse of a ventilated supercavity. *Experimental Thermal and Fluid Science* 79, 294–300.
- Karn, A., Rosiejka, B., 2017. Air entertainment characteristics of artificial supercavities for free and constrained closure models. *Experimental Thermal and Fluid Science* 81, 364–369.
- Karn, A., Chawdhary, S., 2018. On the synergistic interrelation between supercavity formation through vaporous and ventilated routes. *International Journal of Multiphase Flow* 104, 1–8.
- Khadiya, S., Kumari, S., Gupta, R., 2021. Hydrodynamics of Bubble Coalescence in Microchannels. *The Canadian Journal of Chemical Engineering* 99 (5), 1199–1210. <https://doi.org/10.1002/cjce.23918>.
- Kheradmandnia, S., Hashemi-Najafabadi, S., Shojaosadati, S.A., Mousavi, S.M., Malek Khosravi, K., 2015. Development of Parallel Miniature Bubble Column Bioreactors for Fermentation Process. *Journal of Chemical Technology & Biotechnology* 90 (6), 1051–1061.
- Kyriakides, N.K., Kastrinakis, E.G., Nychas, S.G., Goulas, A., 1997. Bubbling from Nozzles Submerged in Water: Transitions between Bubbling Regimes. *The Canadian Journal of Chemical Engineering* 75 (4), 684–691. <https://doi.org/10.1002/cjce.5450750405>.
- Legendre, D., Zenit, R., Velez-Cordero, J.R., 2012. On the deformation of gas bubbles in liquids. *Physics of Fluids* 24 (4), 043303. <https://doi.org/10.1063/1.4705527>.
- Leonard, C., Ferrasse, J.-H., Lefevre, S., Viand, A., Boutin, O., 2021. Bubble Rising Velocity and Bubble Size Distribution in Columns at High Pressure and Temperature: From Lab Scale Experiments to Design Parameters. *Chemical Engineering Research and Design* 173, 108–118.
- Li, M., Hu, L., Xu, H., Chen, W., Xie, H., Fu, X., 2019. Jet Formation during the Gas Penetration through a Thin Liquid Layer. *Physics of Fluids* 31 (1), 017105. <https://doi.org/10.1063/1.5066593>.
- Livinus, A., Verdin, P.G., 2021. Experimental Study of a Single Elongated Bubble in Liquid in under 10-Degree Upwardly Inclined Pipes. *Experimental Thermal and Fluid Science* 120. <https://www.sciencedirect.com/science/article/pii/S0894177720307512> 110247.
- Mohseni, E., Kalayathine, J.J., Reinecke, S.F., Hampel, U., 2020. Dynamics of Bubble Formation at Micro-Orifices under Constant Gas Flow Conditions. *International Journal of Multiphase Flow* 132. <https://www.sciencedirect.com/science/article/pii/S0301932220305164> 103407.
- Muller, R.L., Prince, R.G.H., 1972. Regimes of Bubbling and Jetting from Submerged Orifices. *Chemical Engineering Science* 27 (8), 1583–1592 <https://www.sciencedirect.com/science/article/pii/0009250972800514>.
- Olmos, E., Gentric, C., Vial, C.H., Wild, G., Midoux, N., 2001. Numerical Simulation of Multiphase Flow in Bubble Column Reactors. Influence of Bubble Coalescence and Break-Up. *Chemical Engineering Science* 56 (21–22), 6359–6365.
- Olowson, P.A., Almstedt, A.E., 1990. Influence of Pressure and Fluidization Velocity on the Bubble Behaviour and Gas Flow Distribution in a Fluidized Bed. *Chemical Engineering Science* 45 (7), 1733–1741 <https://www.sciencedirect.com/science/article/pii/0009250990870515>.
- Orvalho, S., Stanovsky, P., Ruzicka, M.C., 2021. Bubble Coalescence in Electrolytes: Effect of Bubble Approach Velocity. *Chemical Engineering Journal* 406. <https://www.sciencedirect.com/science/article/pii/S1385894720320544> 125926.
- Painmanakul, P., Sastaravet, P., Lersjintanakarn, S., Khaothiar, S., 2010. Effect of Bubble Hydrodynamic and Chemical Dosage on Treatment of Oily Wastewater by Induced Air Flotation (IAF) Process. *Chemical Engineering Research and Design* 88 (5), 693–702 <https://www.sciencedirect.com/science/article/pii/S0263876209002743>.
- Park, H., Wang, L., 2015. Experimental Studies and Modeling of Surface Bubble Behaviour in Froth Flotation. *Chemical Engineering Research and Design* 101, 98–106.
- Rajaseenivasan, T., Srithar, K., 2017. An Investigation into a Laboratory Scale Bubble Column Humidification Dehumidification Desalination System Powered by Biomass Energy. *Energy Conversion and Management* 139, 232–244.
- Roig, V., Roudet, M., Risso, F., Billet, A.-M., 2012. Dynamics of a High-Reynolds-Number Bubble Rising within a Thin Gap. *Journal of Fluid Mechanics* 707, 444–466.
- Stover, Richard L, Charles W Tobias, and Morton M Denn. 1997. "Bubble Coalescence Dynamics." *AIChE Journal* 43(10): 2385–92. <https://aiche.onlinelibrary.wiley.com/doi/abs/10.1002/aic.690431002>.
- Wu, H., Wang, B., DiMarco, S.F., Tan, L., 2021. Impact of Bubble Size on Turbulent Statistics in Bubble Plumes in Unstratified Quiescent Water. *International Journal of Multiphase Flow* 141. <https://www.sciencedirect.com/science/article/pii/S0301932221001403> 103692.
- Yang, Weidong, Zhiguo Luo, Qingrui Lai, and Zongshu Zou. 2019. "Study on Bubble Coalescence and Bouncing Behaviors upon Off-Center Collision in Quiescent Water." *Experimental Thermal and Fluid Science* 104: 199–208. <https://www.sciencedirect.com/science/article/pii/S0894177718317801>.
- Yoon, K., Li, J., Shao, S., Karn, A., Hong, J., 2021. Investigation of Ventilation Demand Variation in Unsteady Supercavitation. *Experimental Thermal and Fluid Science* 129, 110472. <https://doi.org/10.1016/j.expthermflusci.2021.110472>.
- Zhou, Y., Ji, B., Zhao, C., Bo, H., 2021. Bubble Formation from a Submerged Orifice in a Thin Liquid Layer: Detachment and Bursting. *Physics of Fluids* 33 (1), 13305. <https://doi.org/10.1063/5.0036330>.